



Focus-diverse, empirical PSF models for the ACS/WFC

Andrea Bellini, Jay Anderson, & Norman A. Grogin

November 20, 2018

Space Telescope Science Institute, 3700 San Martin Drive, Baltimore, MD 21218

Abstract

Focus variations, primarily due to uneven Sun heating of the telescope tube, have a significant impact on the shape of the ACS/WFC point-spread function (PSF). These variations can be properly accounted for on an image-by-image basis by perturbing the library PSF models (Anderson & King 2006) when many bright, relatively isolated stars are present: a luxury that many HST users do not enjoy. This report presents an exploratory analysis of these focus variations and describes the procedures to obtain focus-diverse, spatially-variable PSF models from `_flc` ACS/WFC images taken with the two most commonly used filters: F606W and F814W. The new PSF models are shown to be superior to the library PSF models, particularly when the focus level is extreme, and provide results comparable to those obtained by PSF-perturbation techniques without the need for populated stellar fields in an image. Future analyses will comprise the construction of focus-diverse PSF models for the several other commonly used filters of the ACS/WFC and their implementation in the `hst1pass` reduction package.

1. Introduction

The relatively stable environment of low Earth orbit allows the *Hubble Space Telescope*'s (*HST*'s) Point-Spread Functions (PSFs) to be extremely stable and offer superior astrometric and

¹Copyright © 2003 The Association of Universities for Research in Astronomy, Inc. All Rights Reserved.

photometric quality with respect to any ground-based facility. The current, state-of-the-art, static library of empirical PSF models for the Wide-Field Channel (WFC) of the Advanced Camera for Surveys (ACS) are discussed in detail in Anderson & King (2006). These PSFs are supersampled by a factor of four with respect to the ACS/WFC pixels, and map spatial variations across each CCD using a 9×5 array (see Fig. 1). The best PSF model for a given location on a CCD can be obtained through bi-linear interpolation of the four surrounding PSFs of the array. The fraction of light in the core of the library PSFs varies by $\sim \pm 3.7\%$ with respect to the average PSF computed over the entire WFC. The central pixel of the average PSF contains around 20% of the total star light.

Even though the Earth’s atmosphere has no effect on the *HST* PSFs, periodic focus variations cause the fraction of light in the core of the PSFs to change by up to 5%. This is due to the so-called ‘breathing’: uneven heating of the telescope tube by the Sun as *HST* enters or exits the Earth’s shadow, or it changes orientation relative to the Sun (see, e.g., Sahu, Lallo, & Makidon 2007; Di Nino et al. 2008). This causes focus variations greater than $6 \mu\text{m}$ over timescales of less than a week.

On timescales longer than a month or so, temperature variations average out. But there can still be longer-term focus variations, caused for example by outgassing of the spacecraft which leads to a progressive shrinking of the metering truss (Di Nino et al. 2008). As a result, the secondary mirror is constantly moving toward the primary, and secondary-mirror moves are commanded when needed to compensate for this trend (Di Nino et al. 2008).

As already pointed out in Anderson & King (2006), the library PSFs can be perturbed on an image-by-image basis to account for these focus changes. The perturbation of the library PSFs is now a common practice in high-precision stellar-population studies of dense star systems (e.g., Bellini et al. 2017 and references therein), but it requires the images to always contain at least a few hundred relatively bright and isolated stars: a luxury that many *HST* users do not enjoy.

Recently, Anderson & Bedin (2017) explored the feasibility of deriving a focus-diverse set of spatially-variable PSF models for the Uv-VISible (UVIS) channel of the Wide-Field Camera 3 (WFC3) detector on-board the *HST*. The authors made use of several hundred images of the globular cluster M4 taken with the F467M filter, and demonstrated that it is indeed possible to characterize the time dependence of the shape of the PSFs using a one-parameter family of PSFs regulated by telescope focus. The authors also show that just a handful of stars in an image (compared to the few hundred stars required for perturbation) are sufficient to pinpoint the best focus-diverse PSF model for a given exposure. If the ACS/WFC PSFs can also be easily characterized as a function of focus, then it will be also possible to empirically construct a set of both spatially- and focus-diverse, high-quality PSF models for the filters of the ACS/WFC. Clearly, having access to a set of focus-diverse PSF models for the ACS/WFC would be a great benefit to the entire astronomical community.

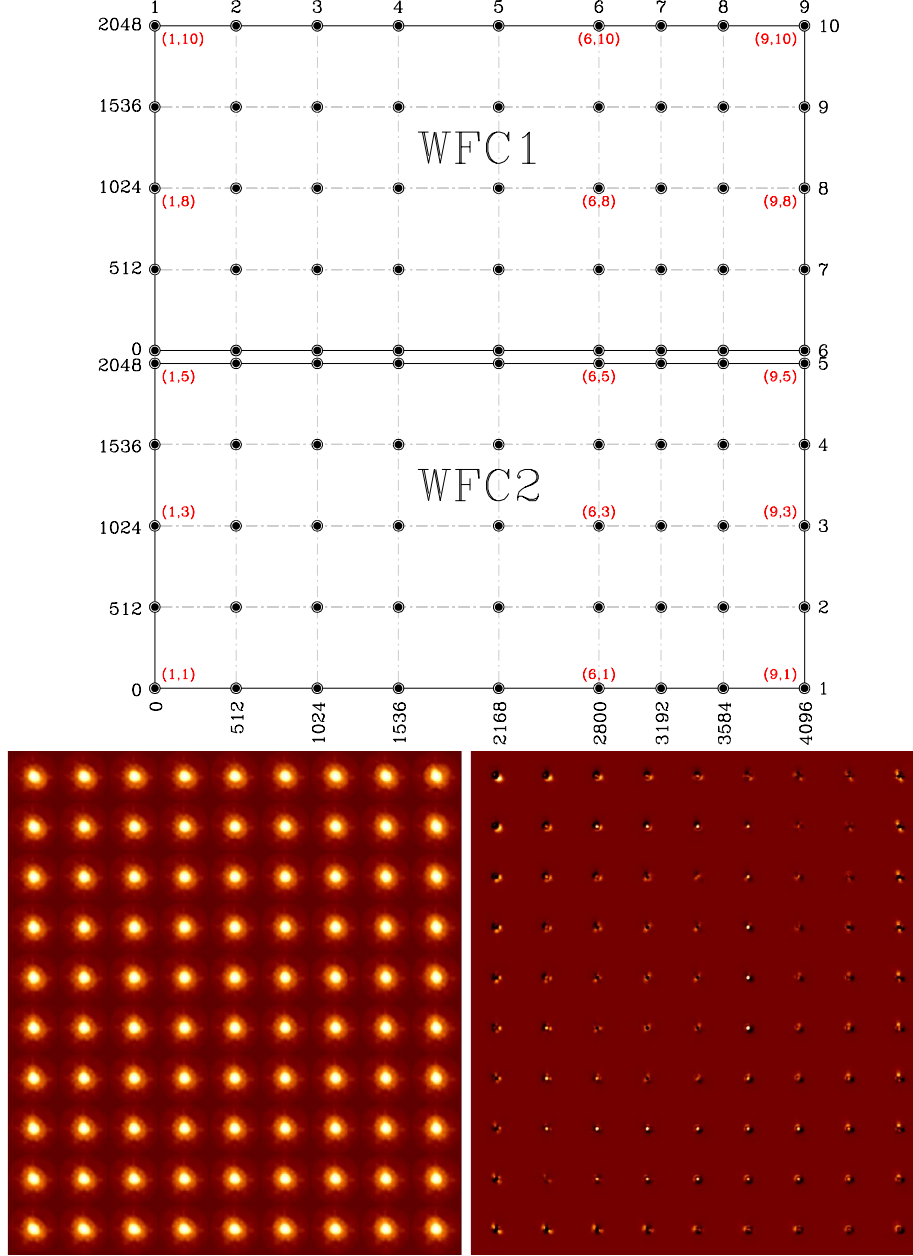


Fig. 1.— (Top:) location of the 9×10 PSF models on the two WFC CCDs, according to the recipes of Anderson & King (2006). Red marks denote a few key locations that will be used later to show focus-dependent variations. (Bottom-left:) 9×10 PSF models of the F606W filter in logarithmic z-scale. (Bottom-right:) the local difference with respect to the average PSF, shown using a linear zscale. Dark (bright) pixels mean less (more) flux in the local PSFs with respect to the single PSF averaged over the entire detector. Pixel variations range from -3.8% to $+3.6\%$.

Table 1

LIST OF PRE-QUALIFYING ACS/WFC IMAGES[†]

Total number of ACS images	183128		
Total number of ACS/WFC full frames	103801		
Short exposures ($30\text{ s} < t_{\text{exp}} < 337\text{ s}$)	4587		
Long exposures ($t_{\text{exp}} \geq 337\text{ s}$)	83542		
Filter	Total	pre-SM4	post-SM4
F435W	4690	2570	2120
F475W	4752	1779	2973
F502N	594	258	336
F550M	412	238	174
F555W	2249	1730	519
F606W	13352	7016	6336
F625W	1485	1178	307
F658N	2408	1188	1220
F660N	8653	2609	6044
F775W	8972	7294	1678
F814W	25580	11989	13591
F850LP	8837	6380	2457
F892N	8	8	0

[†] Public data available at the end of 2017.

In bold the filters analyzed in this work.

2. Sifting through the *HST* archive

A large number of full-frame ACS/WFC exposures are needed to construct focus-diverse PSF models, to allow the mapping of even extreme (and uncommon) focus positions with adequate statistics. In addition, images need to contain enough (at least 300 or so) bright ($S/N \gtrsim 30$), relatively isolated¹ and unsaturated stars (hereafter, the “good” stars), so that high-fidelity, spatially-variable PSF models can be constructed free of pixel-phase errors (see, e.g., Anderson & King 2000).

At the end of 2017, out of the 103,801 publicly available ACS/WFC full-frame images, there were 88,129 with suitably long exposure times (≥ 30 seconds). Because of small but significant changes in both the ACS/WFC geometric distortion and the PSF shape after the camera was repaired during *HST* Servicing Mission 4 (SM4) in 2009 (more later), the PSF analysis has been performed separately for pre- and post-SM4 WFC images. Table 1 shows the total number of full-frame ACS/WFC images available for each filter. The F606W and F814W filters are by far

¹Isolated stars are defined as those sources with no brighter neighbor within 12 pixels.

the most utilized, and therefore the first choices in the filter-by-filter PSF analysis. Future reports will focus on other commonly-used filters.

3. Choosing the right images

Starting with the 7016 pre-SM4 full-frame F606W images, the next step is to identify those among them containing at least 300 good stars. This was accomplished by modifying the software package `hst1pass`—a soon-to-be-released consolidation of several photometric-reduction tools developed by J. Anderson for *HST* cameras—to execute on the WFC raw-format fits files. This software runs a single wave of source finding and performs PSF-fitting photometry using the empirical library PSF models described in detail in Anderson & King (2006).

Figure 2 shows a histogram of the number of bright sources found in each exposure. The quality-of-fit (QFIT) parameter ² of `hst1pass` discriminates between stars ($0 < \text{QFIT} < 0.25$) and extended sources, blends, and cosmic ray detections, all characterized by higher QFIT values. The QFIT parameter indicates how well a source has been fit with the PSF models (See Anderson et al. 2008). QFIT values close to zero mean that the PSFs and the stars have very similar shapes (a value of zero implies a perfect match). The higher the QFIT values, the more discordant the shape of the PSF is from that of the fitted source. Finally, saturated sources are defined as those with a central pixel containing more than 40,000 ADUs. The histogram in Fig. 2 is color-coded according to the fraction of stars (green), extended sources (blue), and saturated stars (red) found in each exposure.

For the 2015 pre-SM4 images containing at least 300 good stars, each was then processed with the ACS calibration pipeline `CALACS` to produce dark, bias, flat-field and CTE-corrected `_flc` images.

4. The pre-SM4 F606W Phylogram

The software `hst1pass` is run again, this time only on these 2015 `_flc` images. In addition, at odds with the previous run, `hst1pass` perturbed the library PSFs using the good stars found in each image. The perturbation array is designed to vary between a single perturbed PSF up to 5×5 perturbed PSFs across the ACS/WFC full frame. Different regions of a full-frame ACS/WFC exposure are affected differently by changes in focus (more in Sect. 5), so the 5×5 perturbation array is the preferred choice to better reproduce the effects of focus variations. At least 20 good stars are needed per perturbed PSF in the array, to mitigate low-number statistics effects.

²The QFIT is defined as the sum over the fitting aperture of the absolute difference between the pixel values $\text{pix}_{i,j}(\text{sky subtracted})$ and the scaled PSF values $\psi_{i,j}$, normalized by the pixel values: $\sum_{i,j} \frac{|\text{pix}_{i,j} - \text{sky} - Z \times \psi_{i,j}|}{\text{pix}_{i,j} - \text{sky}}$, where Z is the flux of the source within the fitting aperture.

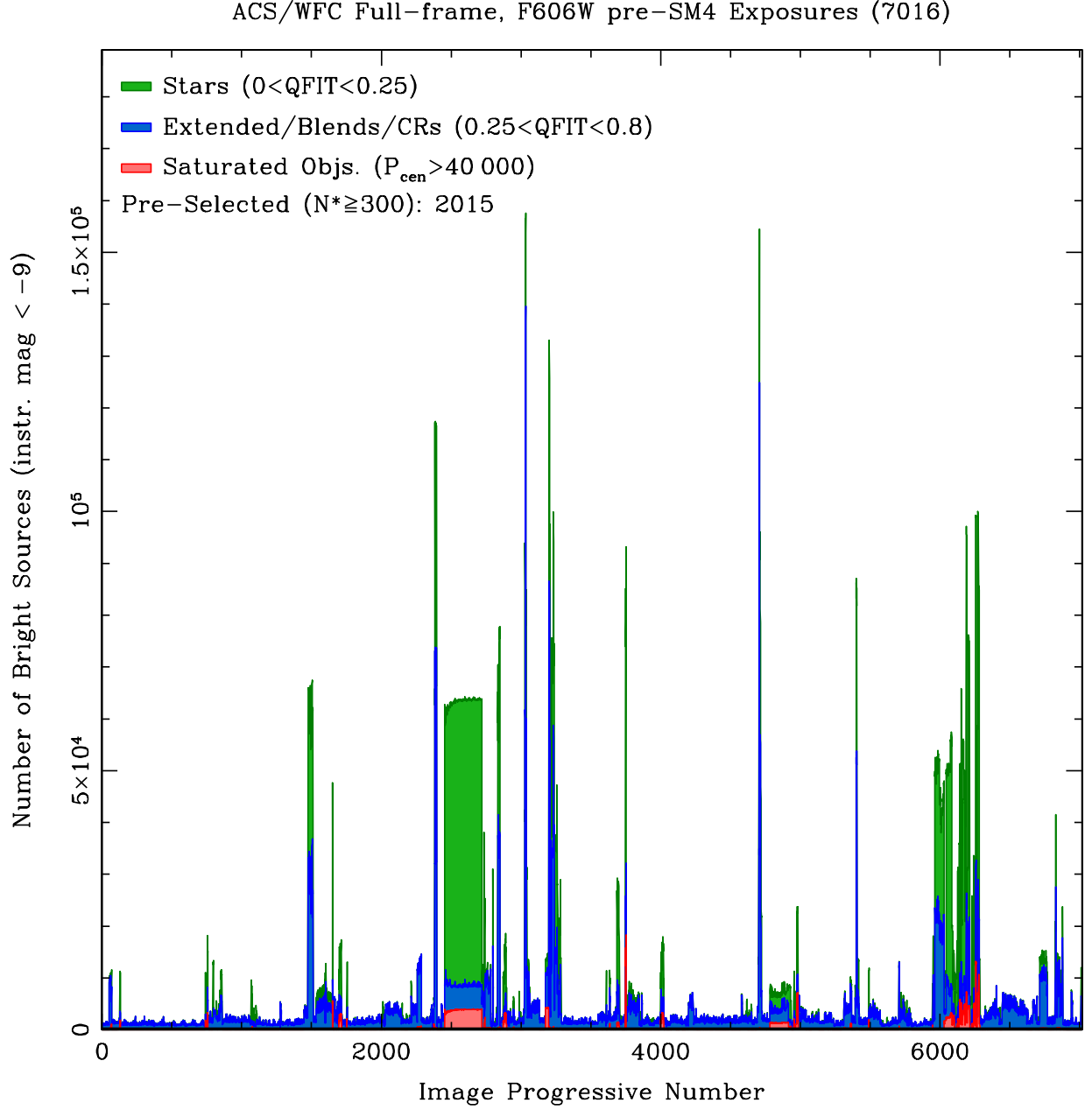


Fig. 2.— Histogram of the number of bright sources ($S/N \gtrsim 30$) measured on the 7016 full frame, pre-SM4 F606W ACS/WFC `raw` exposures. Saturated sources are in red. Extended sources, blends and cosmic-ray detections are in blue. Well-measured stars are in green.

These selections resulted in 1347 exposures that were used to construct 5×5 perturbation PSF arrays. For each of these images, the good stars are fitted with the library PSFs appropriate for their location in the image. The library PSFs are then subtracted, and the residuals are

averaged over each region in the image and collected into the perturbation array. The perturbation array is then projected into the 9×10 array space of the library PSFs, and summed to the library PSFs themselves to obtain a new set of 9×10 improved PSFs for that particular image. The process is iterated and, at each iteration, the residuals of the PSF fit become increasingly smaller, implying that the new PSF models are converging to match the actual shape of the stars in that image. Convergence is reached when the difference in the residuals from one iteration to the next is smaller than $< 10^{-4}$.

The next step is to construct the so-called “phylogram” plot, following the recipes described in great detail in Anderson & Bedin (2017). The phylogram is a two-dimensional plot that represents multidimensional differences between the image-tailored PSFs in terms of differences between points in a two-dimensional space. Phylograms are commonly used in biology (in particular, in phylogenetics) to highlight differences between species in terms of the total difference of their DNA code. In the current study, for each image pair i, j , the quantity $d_{i,j}$ gives the normalized sum of the absolute value of the differences between the pixels of the 9×10 array of PSFs. Two images with similar (different) PSFs will have a small (large) $d_{i,j}$ value. The phylogram plot is populated by adding one point at a time, where each point corresponds to one of the 1347 images. The first point is placed at the origin (0,0). The second point can be placed anywhere on a circle of radius $d_{1,2}$ around the first point. Once the second point is placed, the third point can be placed in only two positions on the phylogram that are $d_{1,3}$ away from the first point, and $d_{2,3}$ away from the second point. Starting from the fourth point, there are no exact solutions, and the location of each of the already-placed points is allowed to slightly adjust itself in such a way as to minimize the sum of all placement errors. (see Anderson & Bedin 2017 for an in-depth description of the method).

Figure 3 show the phylogram of the 1347 pre-SM4 F606W images. At odds with the phylogram Anderson & Bedin (2017), which is based WFC3/UVIS F467M exposures (their Fig. 5), the phylogram in Fig. 3 is clearly bi-modal on one side, with an inner and an outer ‘bend’, and presents significant spread that is not related to placement errors (red points and inset in Fig. 3). The ACS/WFC is located off-center on the focal plane, while the WFC3/UVIS is at the center of the focal plane: this could play some role in producing the differences between the WFC3/UVIS and the ACS/WFC phylograms.

Accurate focus models³ can be obtained for most of the 1347 images shown in Figure 3. The temperature-dependent part of these models come from Di Nino et al. (2008), while the long-term secular component is based on Niemi et al. (2010). Figure 4 illustrates the relationship between the average focus models and the pre-SM4 F606W phylogram. The position of the secondary mirror of *HST* was adjusted three times between the installment of ACS and when the camera failed in 2007, in order to account for focus drifts due to outgassing of the spacecraft (Di Nino et al. 2008). The top panels of Fig. 4 show the histograms of the focus models separated into

³www.stsci.edu/hst/observatory/focus/FocusModel

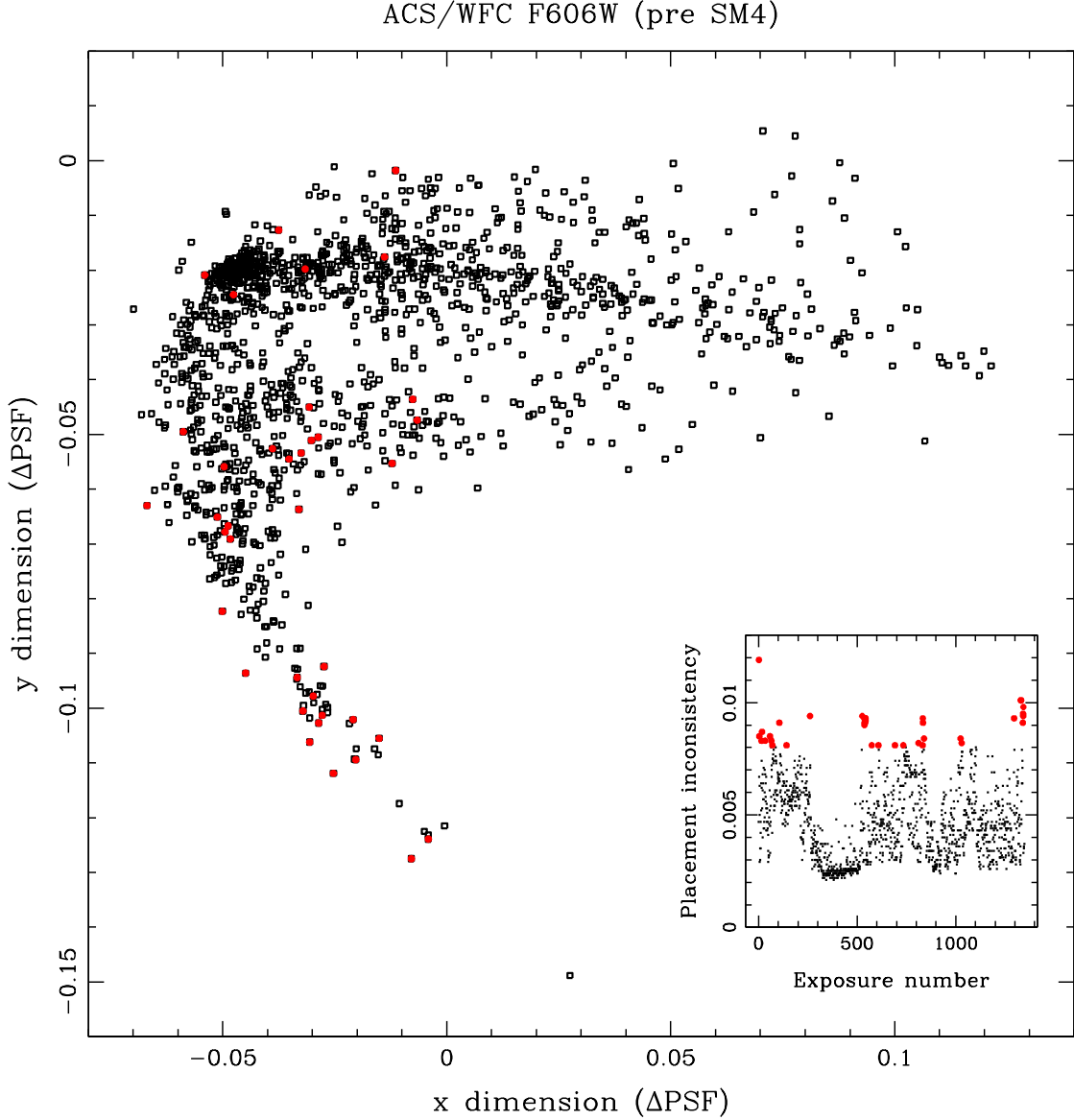


Fig. 3.— (Main panel:) Phylogram of pre-SM4 F606W exposures. Each open square represents an image. The relative distance between squares corresponds to the global absolute difference between their PSFs. The orientation and zero point of the plot are arbitrary. The inset shows the placement error as a function of exposure number. Images with high placement errors are marked in red in both panels, showing no obvious correlations between placement errors and image position on the phylogram.

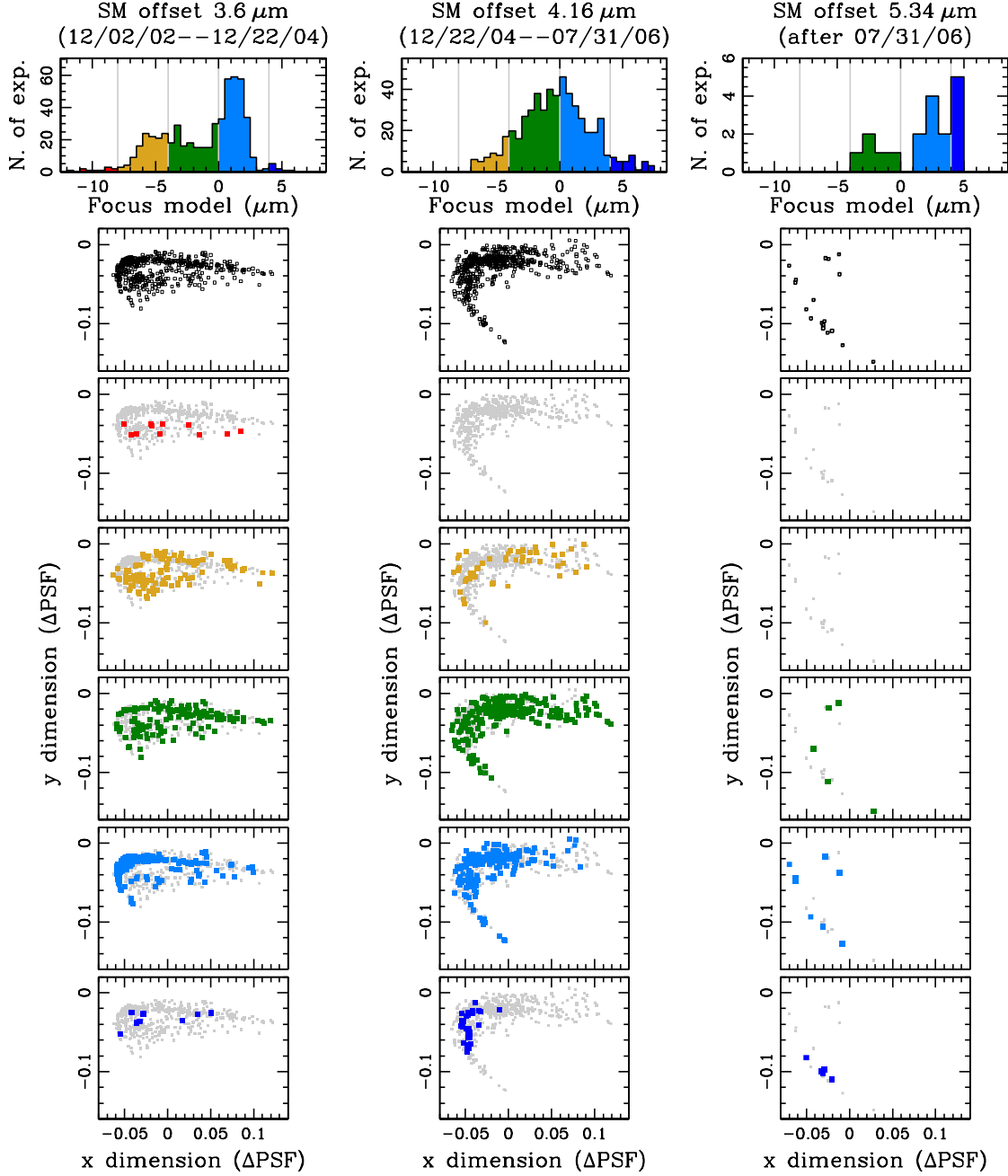


Fig. 4.— On top, the histograms of focus models for pre-SM4 F606W images taken at particular secondary-mirror (SM) offsets. The histograms are divided into 5 groups and color coded from red to blue from the most negative to the most positive groups, respectively. Note that only a few images belong to the red group in the leftmost SM offset, while the red groups of the other two SM offsets are empty. The second row of panels shows the phylogram plots of images taken at the three secondary-mirror offsets. The remaining panels highlight where images of different focus groups are located on the (now grayed out) phylograms.

the time intervals in between secondary-mirror adjustments. The three panels on the second row illustrate the phylogram plots for the same periods, showing that points on the phylogram move progressively to the lower part as the secondary-mirror offset increases.

The focus histograms are divided into 5 groups spaced every $4\ \mu\text{m}$, and color coded from red to blue from the most negative to the most positive groups, respectively. The remaining panels of Fig. 4 show where images of different focus groups are located on the phylogram. Not much can be said about the rightmost panels, due to low-number statistics. For the first two secondary-mirror positions it seems that, on average, images with negative focus levels do not preferentially populate the lower end of the phylogram, which is instead preferentially populated by images characterized by more positive focus values.

To better understand if and how other parameters might be at play in determining the shape of the ACS/WFC phylogram, different telescope and exposure conditions extracted from the image headers are analyzed in Fig. 5. No significant correlations are found with the Moon angle (as expected since the Moon angle does not significantly affect the thermal load on the telescope), nor with the primary-use detector. The points in the phylogram correlate with the angle between the Sun and the V1 axis (Sun angle), with the inner bend being populated by images with larger Sun angles, while the outer bend is less affected.

Early observations are found to mostly populate the inner bend, while the vast majority of the later observations are on the outer bend. Images affected by relatively small jitter RMS are predominantly in the inner bend. It also appears that exposure time affects the location of the PSFs on the phylogram, with shorter exposures predominantly on the outer bend. This can be interpreted as the focus level being almost constant within a short observation, while long observations have sufficient time to map somewhat larger focus variations, resulting in focus-averaged PSFs. Because of the need to accommodate parallel buffer dumps during ACS/WFC full-frame image sequences, WFC observations are typically longer than 337 seconds, to maximize the “on sky” telescope time.

Finally, it appears that the Sun altitude over the Earth limb (Sun alt angle) has also some effect on the location of the PSFs on the phylogram: images characterized by a large Sun alt values preferentially populate the outer regions of both bends.

5. PSF modeling

Since both the location and the orientation of the points in the phylogram are arbitrary, the points are rotated so that their profile resembles a ‘U’ shape, hereafter the reference phylogram (Fig. 6). This phylogram is arbitrarily divided into 18 distinct regions/groups. This is a trade-off between the need of a fine sampling of PSF variations and enough statistics within each sample. The plan is to derive a set of spatially-varying PSF models for each of these regions. These sets will be representative of the full focus variation affecting pre-SM4 F606W exposures.

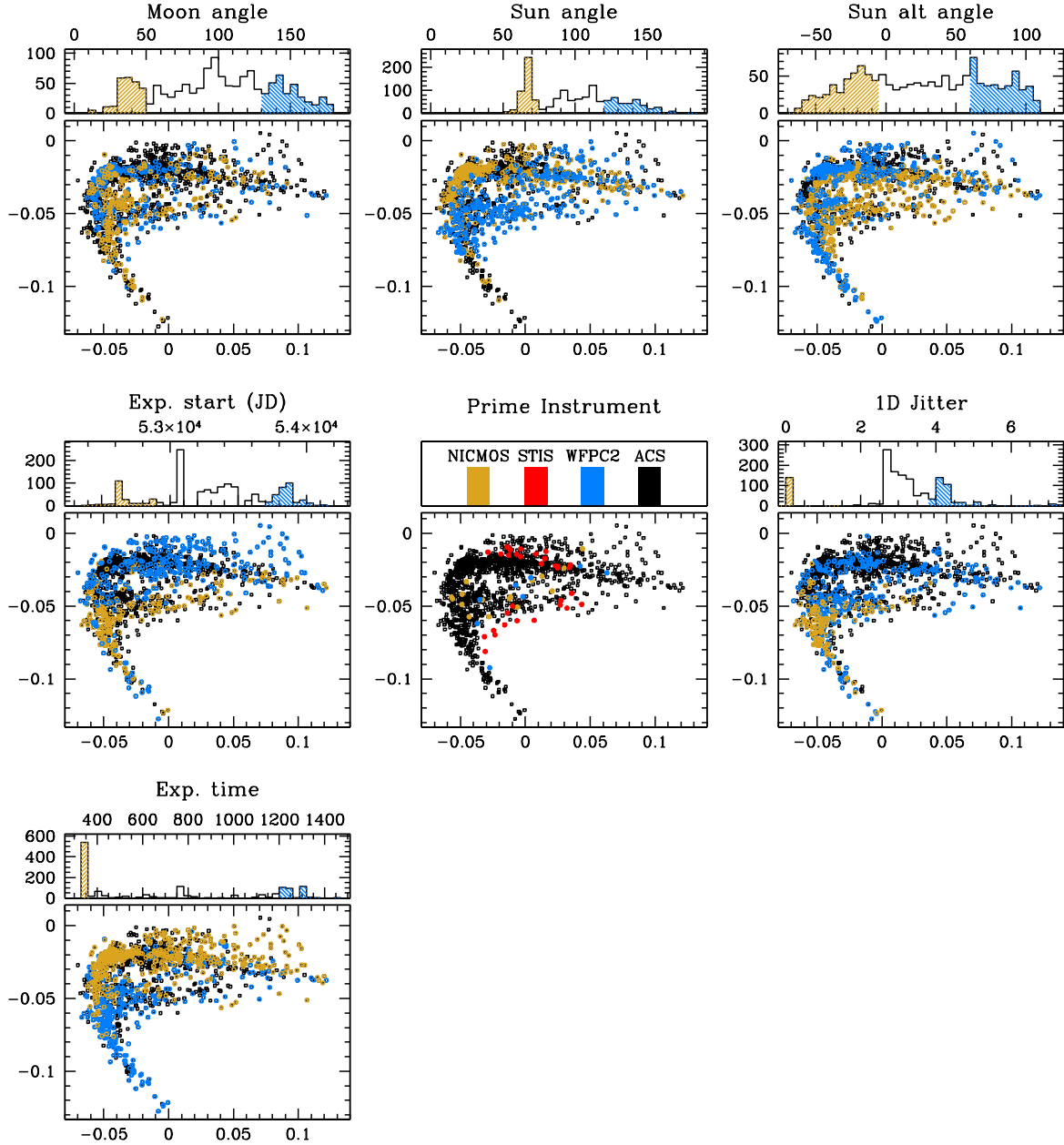


Fig. 5.— These panels illustrate possible correlations between the location of the images on the phylogram and various parameters: Moon and Sun angle with respect to the V1 axis of the telescope, altitude of the Sun above the Earth’s limb, epoch, the primary-use instrument, jitter RMS, and exposure time. See the text for details.

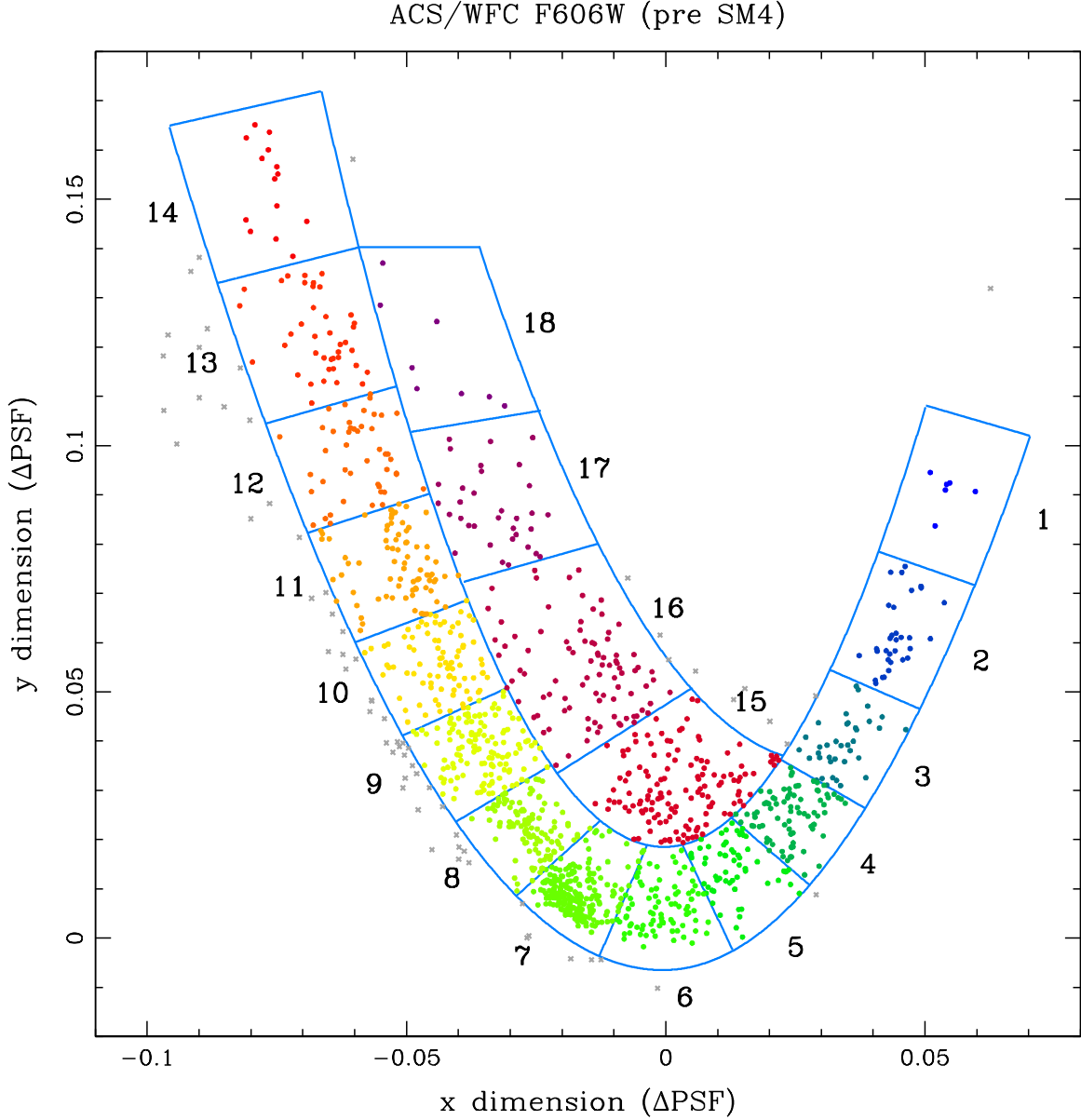


Fig. 6.— Reference phylogram (similar to Fig. 3 but shifted and rotated so that it resembles a “U” shape). The phylogram is divided into 18 distinct regions (focus groups). The images within each region are used to construct 18 sets of spatially-variable, focus-diverse PSF models. The gray points outside the focus regions are considered as outliers and are not used to define the focus-diverse PSF models. These points are reasonably close to one of the focus regions, so that the associated focus-diverse PSF models can still be successfully used for them as well.

Because of the undersampled nature of *HST* detectors, many stars at different sub-pixel positions are necessary to obtain PSF models that are free of pixel-phase errors. This can be achieved either by taking multiple dithered observations of the same field (e.g., Anderson & King 2000), or by using multiple observations of different fields.

Following the prescriptions given in Anderson & Bedin (2017), the construction of the focus-diverse PSF models started by determining preliminary positions and fluxes of stars in the associated images of each group using the available library PSFs. The PSF-fitting residuals were then used to construct an initial array of 9×10 spatially-variable PSF models. With the new PSFs, new and improved stellar positions and fluxes are obtained, which in turn are used to construct improved PSF models. This procedure is very similar to that used in Sect. 4 to derive tailored PSF models to each image. The main advantage here is that many images with similar focus properties are combined at once, providing many more stars to directly constrain the full 9×10 array of PSF models, instead of having to rely on projections from a less-optimal 5×5 perturbation array.

As done in Anderson & Bedin (2017), stellar fluxes are measured through a 5-pixel-radius circular aperture. This accounts for the flux that landed outside the 5×5 -pixel square aperture used by the PSF-fitting routine.

To better illustrate how focus affects the PSF shape, Fig. 7 reports the same reference phylogram space plane of Fig. 6, but this time the points of the 18 regions are replaced by a zoomed-in view of the differences between the central 49×49 pixels of the top-left PSF of the 9×10 array—which is at location (1,10) (see Fig. 1)—with respect to the corresponding library PSF. There is a continuous transformation of the residuals moving from groups 1 to 14. The residuals start from having a cross-like shape in the core, with less flux along one direction and more flux along the perpendicular direction (group 1). Then, they evolve towards a shape more similar to that of the library PSF, but with less flux in the core (groups 7,8), and finally they exhibit more flux in the core but less flux in an annulus just outside the core at the opposite extreme of the focus level (groups 11–14). Groups 15 to 18 on the inner bend show an overall similar (but not identical) residual behavior as groups 6 to 12.

Figure 8 illustrates the focus dependence of the PSF residuals with respect to the library PSF at 14 other array locations (all the remaining locations shown in red in Fig. 1). Again, the shape of the residuals continuously changes when moving from group 1 to group 14, with groups 16 to 18 generally showing similar trends to groups 6 to 12. It is worth noting that, while for instance the residuals of the PSF at location (1,1) start negative in the core and evolve towards positive values, the core of residuals of PSF at location (6,5) starts positive in groups 1–3, then becomes negative in groups 5–10, and returns positive again in groups 11–14. Clearly, focus variations have different effects in different locations of the WFC detector. This is why focus variations cannot be easily de-coupled from spatial variations.

Table 2 lists the peak-to-peak pixel variations of the focus-diverse PSF arrays with respect to

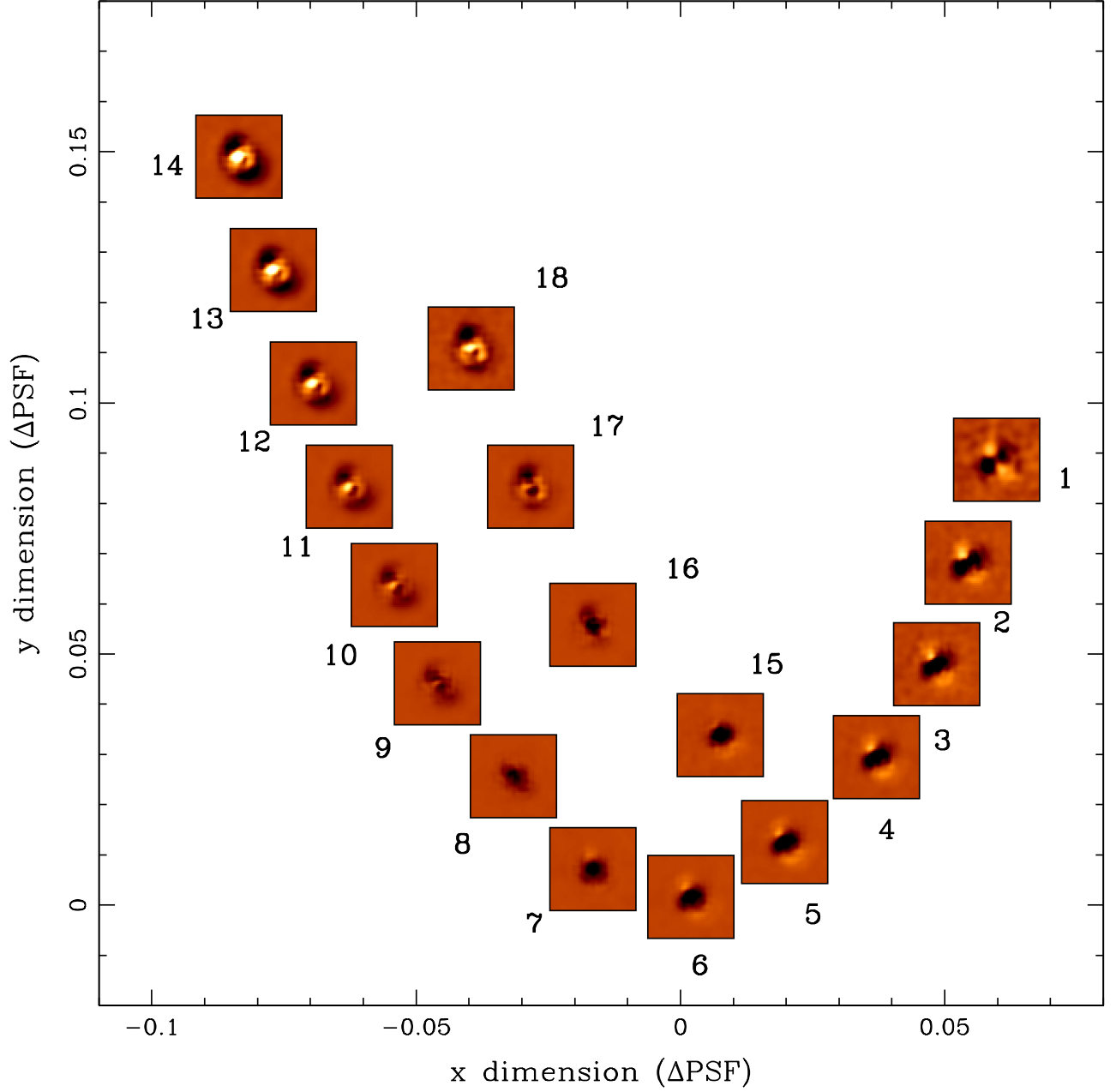


Fig. 7.— Variation of the focus-diverse PSF at location (1,10) —i.e., the top-left PSF of the WFC1 CCD— with respect to the library PSF. Note the smooth and continuous variation from one extreme of the reference phylogram to the other.

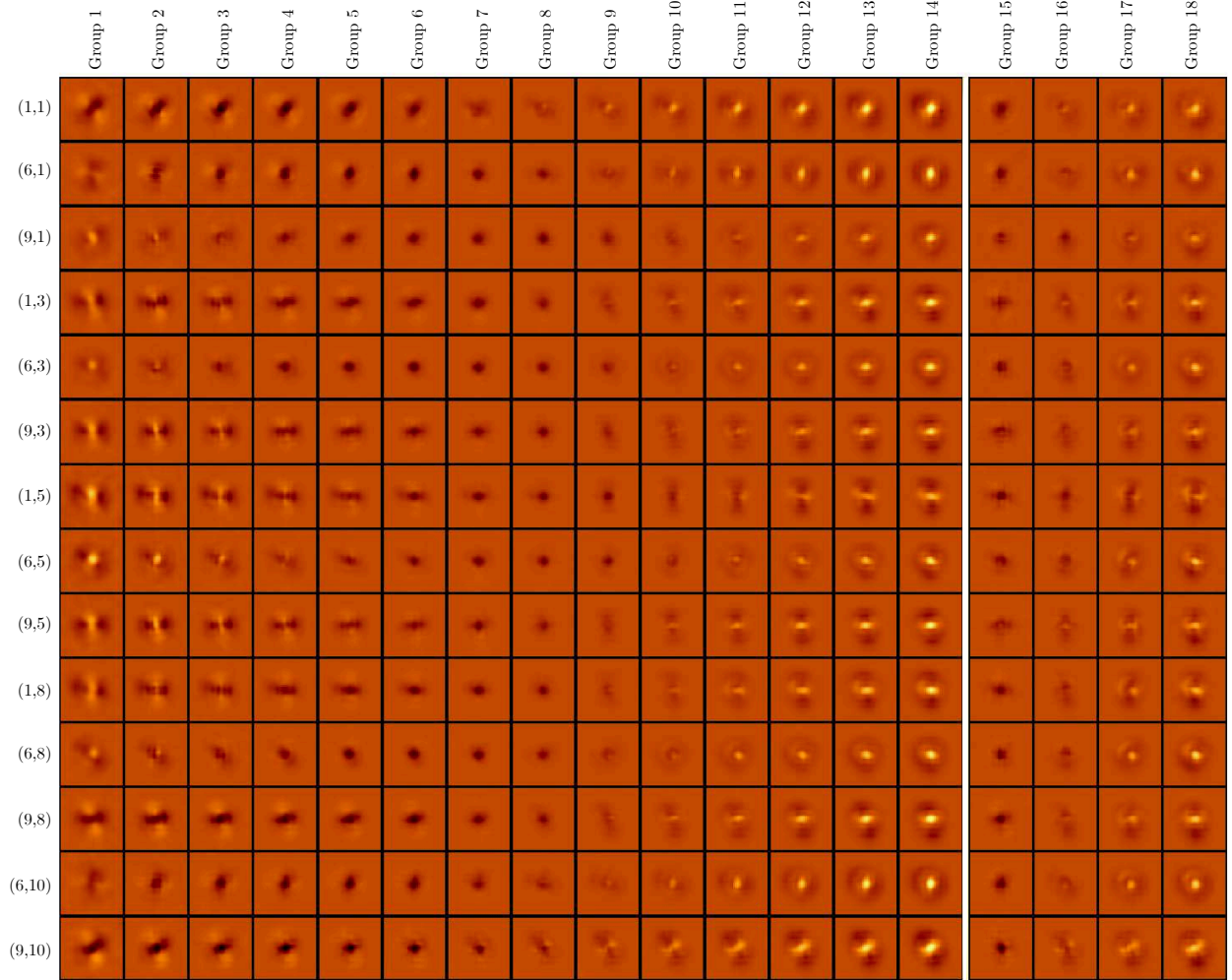


Fig. 8.— Variation of 14 selected PSFs (the same marked in red in Fig. 1 except for PSF (1,10), which is shown in Fig. 7) with respect to the library PSF as a function of focus group.

the library PSFs.

6. Results

One way to test how well the shape of the new focus-diverse PSF models resembles that of the stars in an image is through the analysis of the QFIT parameter. Recently, Hoffmann & Anderson (2017) used the QFIT parameter to demonstrate the superiority of the empirical PSF models over the theoretical TinyTim PSFs (see Fig. 9). In what follows, it is shown that the focus-diverse PSF models derived in the present study are superior to the library of empirical PSFs.

The library PSF models are generally similar to the focus-diverse PSF models of groups 6

Table 2
PEAK-TO-PEAK VARIATIONS OF THE FOCUS-DIVERSE PSFs WITH RESPECT
TO THE LIBRARY PSF AS A FUNCTION OF FOCUS GROUP

Group	Min	Max	Group	Min	Max	Group	Min	Max
1	−3.0%	+4.3%	7	−2.5%	+0.2%	13	−1.1%	+4.0%
2	−3.1%	+2.6%	8	−2.2%	+0.4%	14	−1.2%	+5.7%
3	−3.4%	+1.7%	9	−1.4%	+0.9%	15	−2.6%	+5.1%
4	−3.5%	+0.7%	10	−1.0%	+1.5%	16	−1.2%	+0.6%
5	−3.1%	+0.5%	11	−0.8%	+2.4%	17	−0.9%	+1.8%
6	−2.9%	+0.3%	12	−0.9%	+3.0%	18	−1.0%	+3.5%

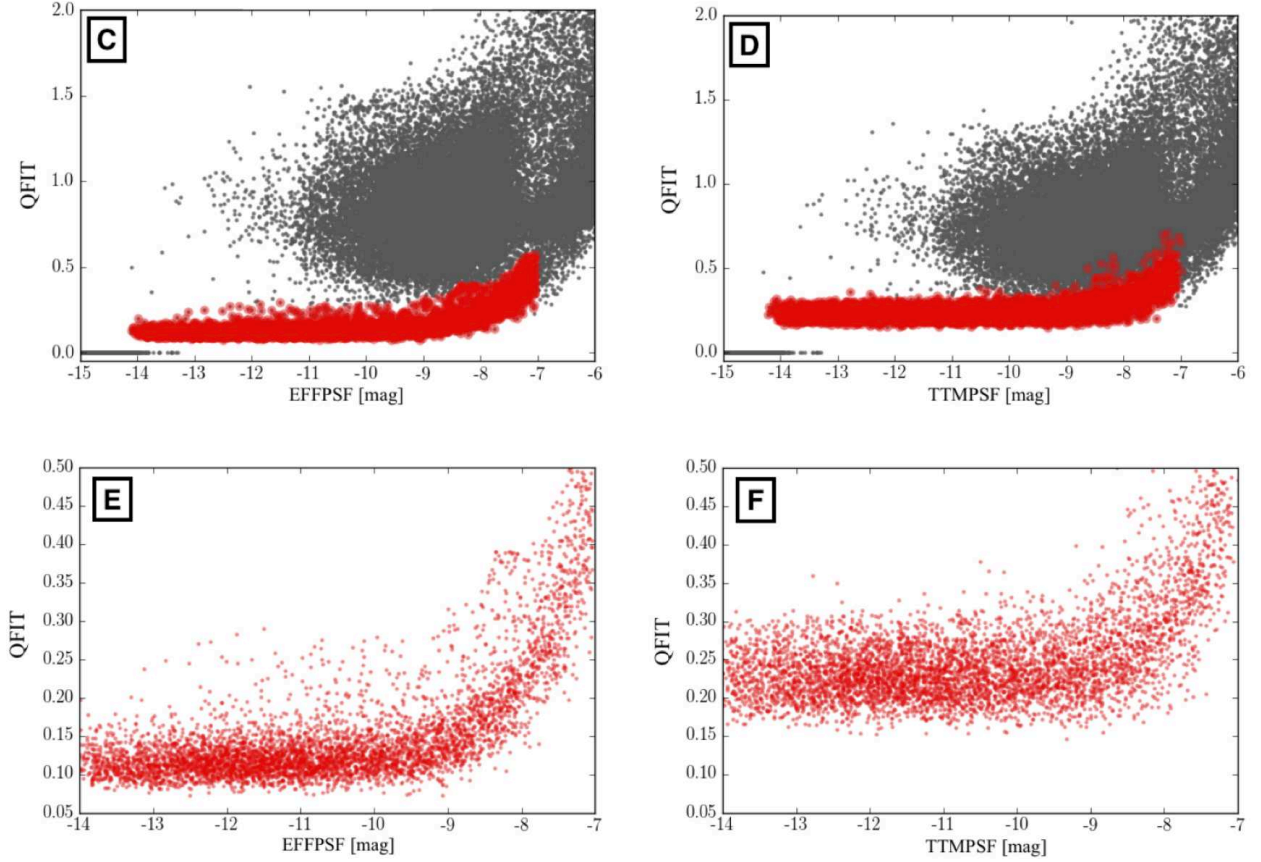


Fig. 9.— Reproduction from Hoffmann & Anderson (2017, their Fig. 4). The panels show a comparison of the QFIT parameter as a function of instrumental magnitude for sources measured on the same image using the library PSFs (EFFPSF, left) and Tiny Tim PSFs (TTIMPSF, right). Well-measured sources are in red.

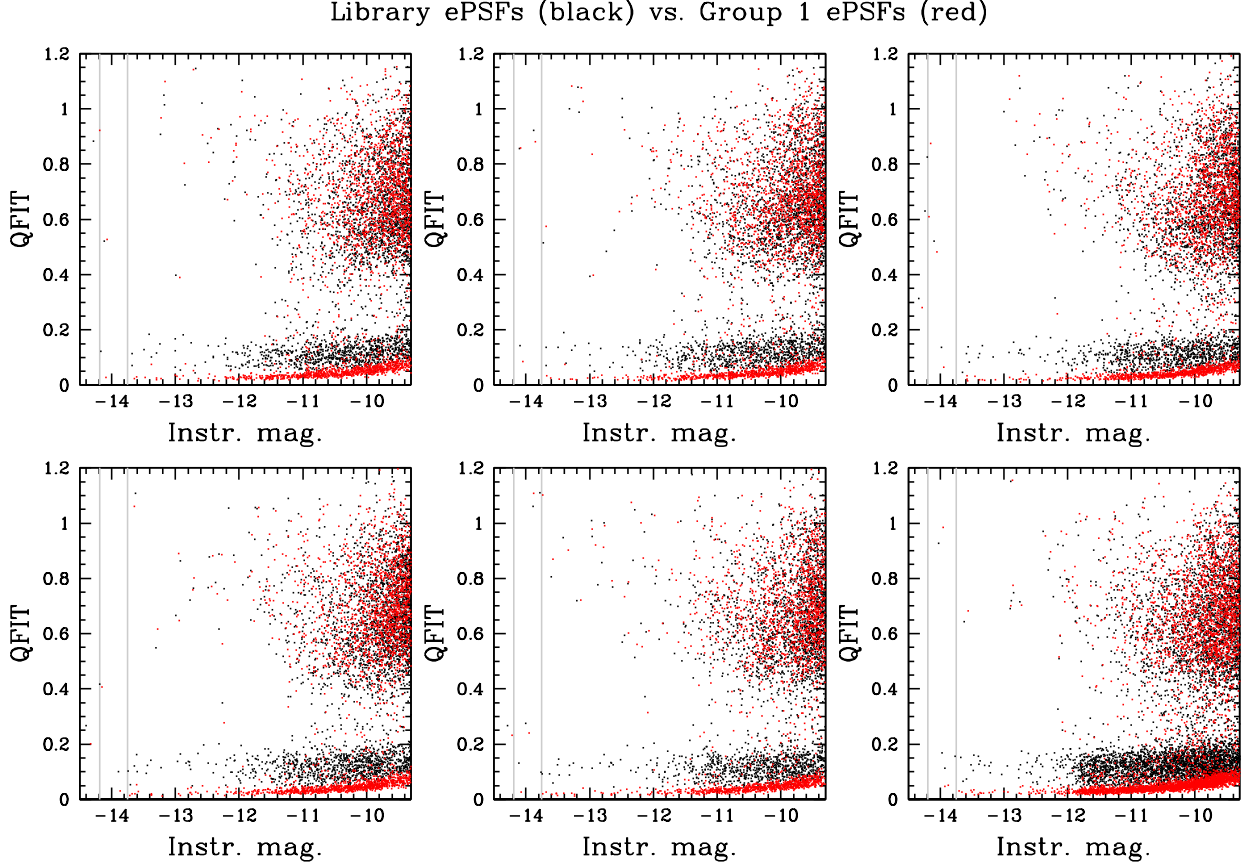


Fig. 10.— Comparison of the QFIT parameter as a function of instrumental F606W magnitude for six images in the focus group 1 as measured by the library PSFs (black) and the focus-diverse PSFs (red).

to 10, so the QFIT values of images belonging to these focus groups are not expected to be much different. In fact, only marginal improvements are found using the focus-diverse models. On the other hand, the difference between the focus-diverse and library PSF models is maximized for the extreme groups 1 and 14. A set of six randomly-selected images in these two extreme groups are used to measure the QFIT parameter of their sources (Figs. 10 and 11 for groups 1 and 14, respectively) via library PSF fitting (black) and focus-diverse PSF fitting (red). In both figures, the QFIT values of well-exposed stars measured by the library PSFs is as high as 0.15–0.2, while the average QFIT value for the focus-diverse measurements is 0.05 or less. The two gray vertical lines in the figures mark the range of the saturation onset, which varies spatially across the WFC field of view.

QFIT values $\lesssim 0.05$ are generally consistent with what is achievable by perturbing the library PSFs on an image-by-image basis, but this task requires an abundance of bright, isolated stars in each image. Here the focus-diverse models are simply applied without perturbation. The

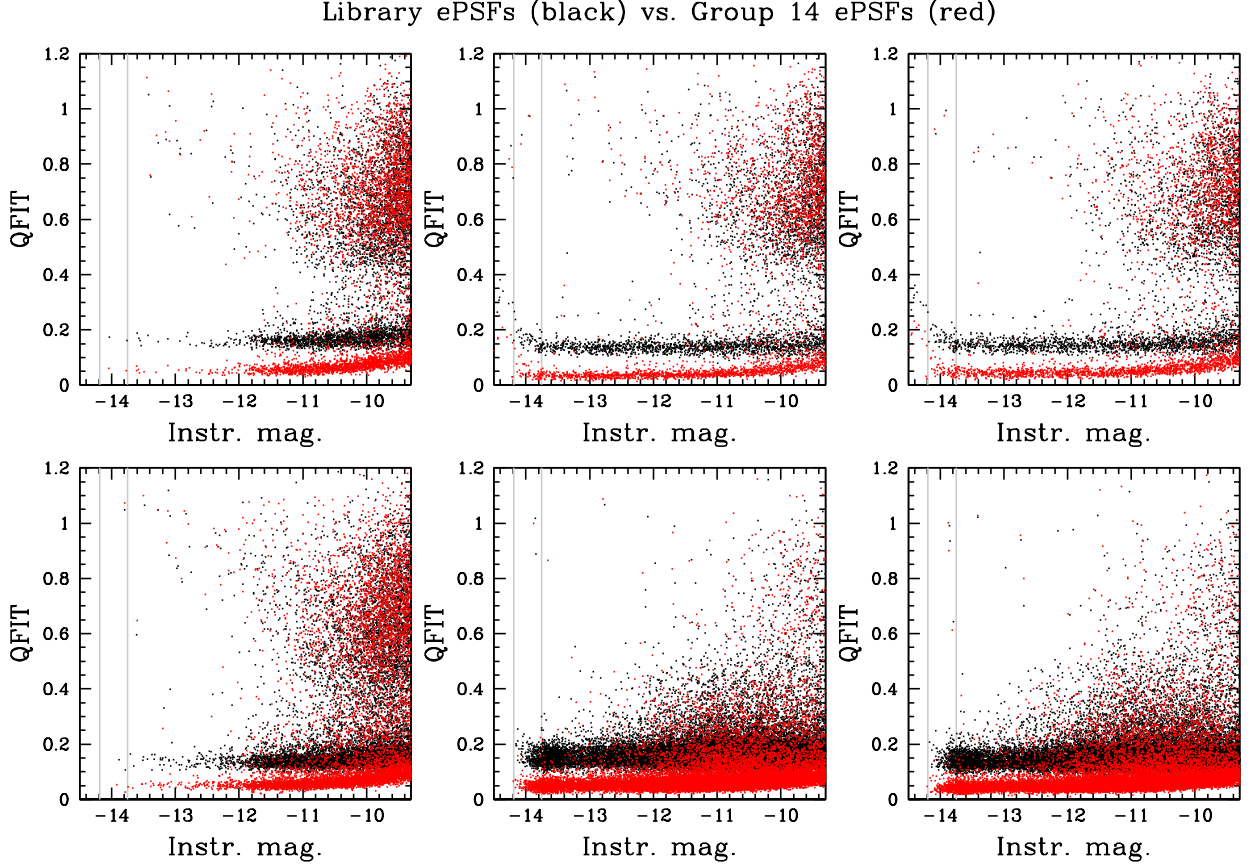


Fig. 11.— Similar to Fig. 10 but for six random images in the focus group 14.

improvement with respect to the library PSFs is clear.

When many stars are also available, it is possible to further refine the focus-diverse PSF models via PSF perturbation. To show this, stellar positions and fluxes of sources are measured for the image `j9it02i6q_flg.fits` (focus group 14, see Fig. 12) using the library PSFs (black), the focus-diverse PSFs (red), and by perturbing the focus-diverse PSFs using a 5×5 perturbation array (blue). The top panel of the figure shows **QFIT** values versus instrumental magnitudes for the three measuring methods, illustrating the further improvement offered by PSF perturbation.

Most importantly, the lower panels in Fig. 12 highlight the presence of pixel-phase errors when the library PSF models are used under extreme focus level conditions. Since stars in the image are at random sub-pixel locations, their measured positions should uniformly populate the pixel-phase space. The figure shows that this is not the case when stars are measured with the library PSFs. The core of the library PSFs is too shallow and results in non-negligible systematic effects in the measured stellar positions. Stars measured with the focus-diverse PSF models, on the other hand, do a much better job in mitigating pixel-phase systematic errors: a clear advantage

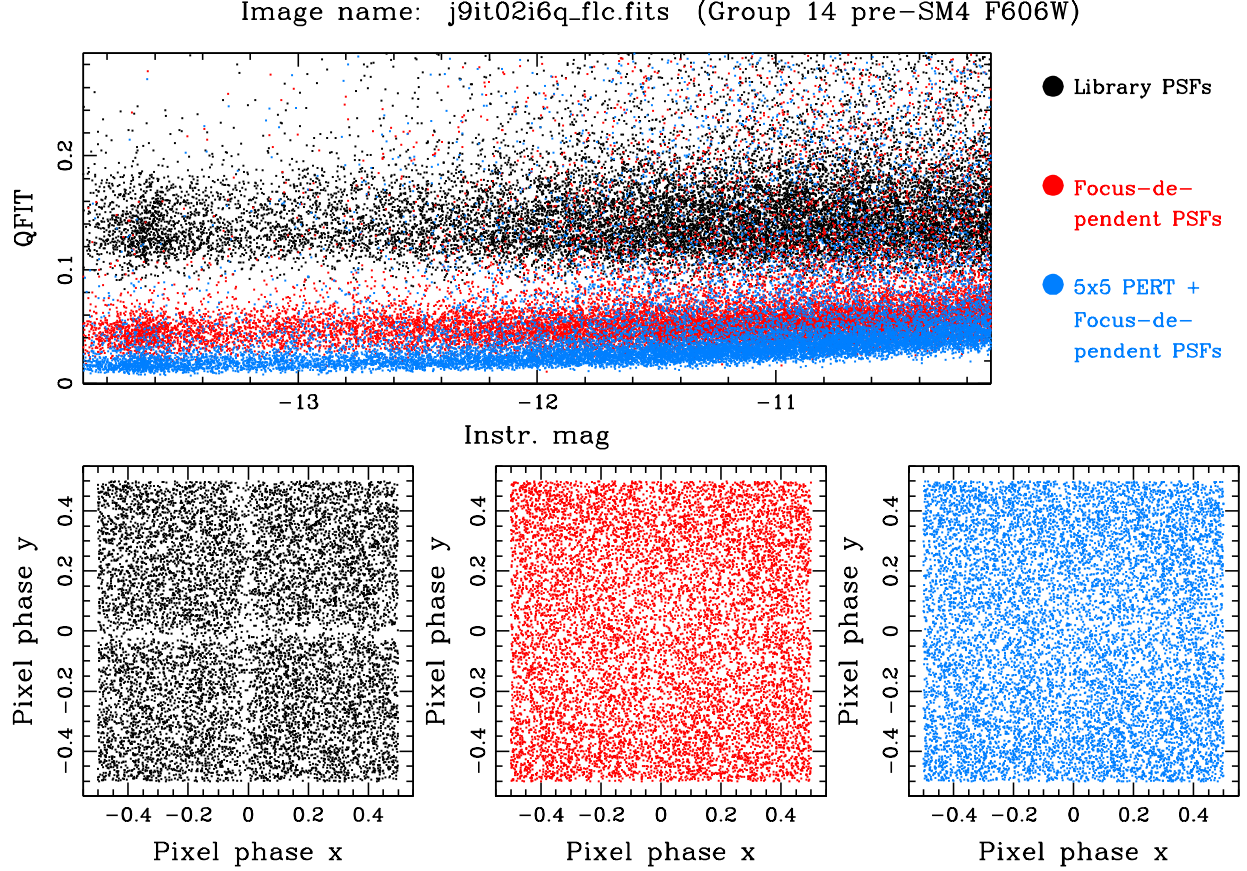


Fig. 12.— (*Top*:) the QFIT versus instrumental magnitude for sources in one of the images in the focus group 14 as measured by the library PSFs (black) the focus-diverse PSFs (red), and by perturbing the focus-diverse models (blue). (*Bottom*:) Pixel-phase space distribution of sources measured with the library PSFs (left, in black), the focus-diverse PSFs (center, in red), and the perturbed focus-diverse PSFs (right, blue).

for astrometric applications (see, e.g., Bellini et al. 2014).

The analysis presented thus far has comprised only pre-SM4 F606W images but, as part of this study, new focus- and spatially-variable PSF models are also obtained for post-SM4 F606W images, as well as for the F814W filter (both pre- and post-SM4). The left panel of Fig. 13 shows the phylogram plot for post-SM4 F606W observations, to be compared to that for pre-SM4 observations in Fig. 3. As for the pre-SM4 phylogram, Fig. 13 also exhibits a multi-modal distribution of points on one side, the locations of which do not correlate with the placement errors of the phylogram-construction process (inset). As for the pre-SM4 case, correlations are found between the different phylogram bends and the angle between the Sun and the V1 axis, the exposure time, the epoch of observation, and the Sun altitude above the Earth’s limb. No correlations are found for the other parameters shown in Fig. 5.

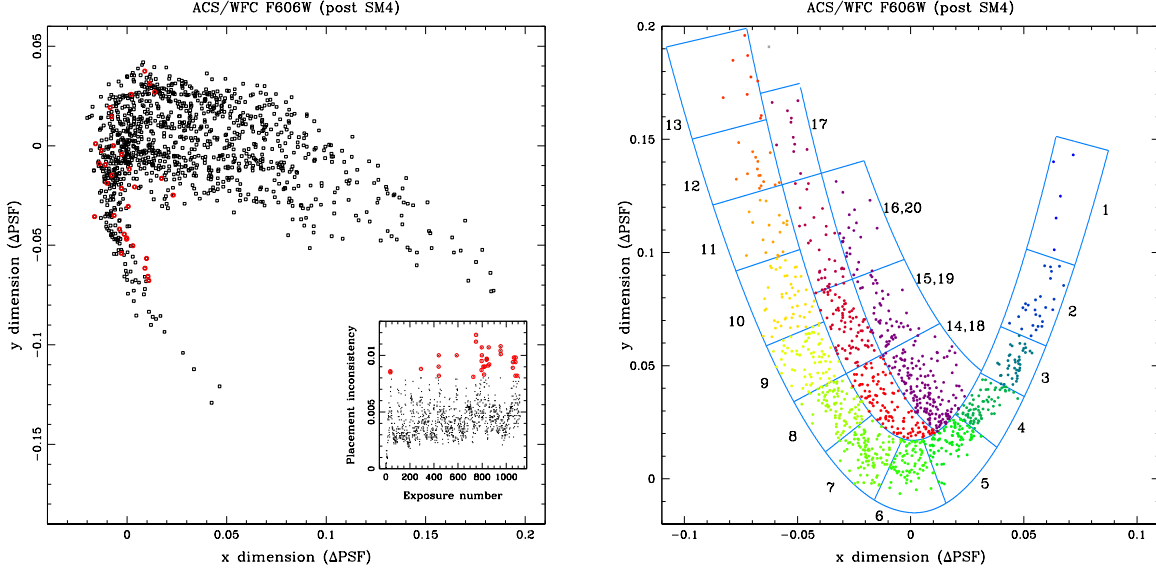


Fig. 13.— Similar to Fig. 3 (left) and Fig. 6 (right) but for post-SM4 F606W images.

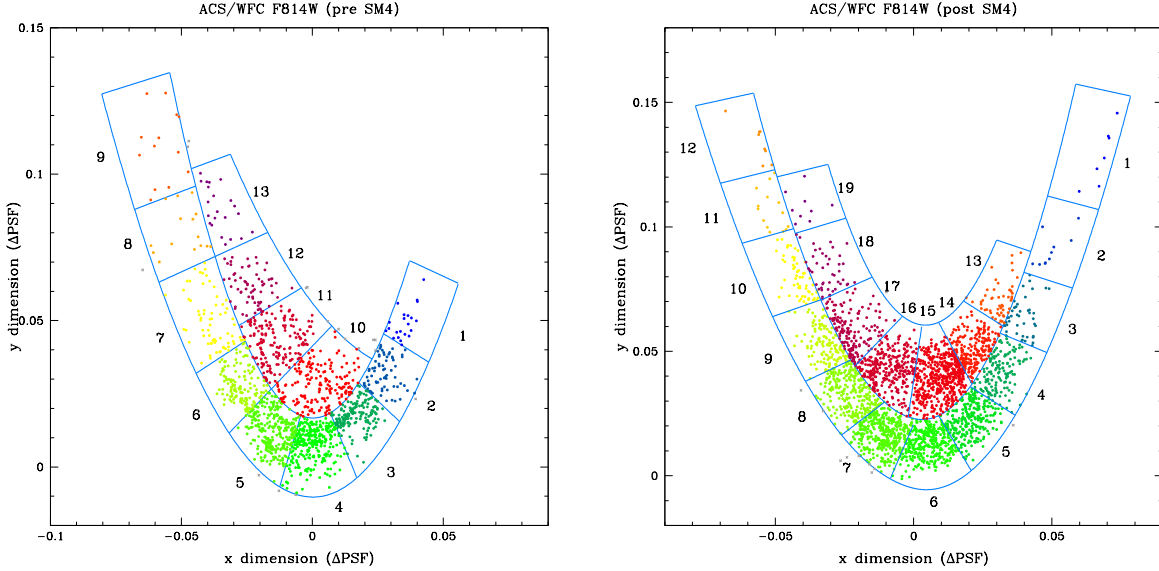


Fig. 14.— Similar to Fig. 6 but for pre- (left) and post-SM4 (right) F814W images. Note the clear difference between the two phylograms.

On the right panel of Fig. 13 the reference post-SM4 F606W phylogram is divided into 20 arbitrarily-defined focus groups. Note the differences between the shape of the pre- and post-SM4 reference phylograms of the F606W filter (Figs. 13 versus 6). The pre-/post-SM4 difference of the

ACS/WFC reference phylograms is even clearer for the F814W filter in Fig. 14, as a consequence of a general PSF shape change of the ACS/WFC after SM4.

The focus-diverse PSF models of the post-SM4 F606W images, as well as of the pre- and post-SM4 F814W images provide similar improvements with respect to the library PSFs as those described above for the pre-SM4 F606W images.

7. Conclusions

The present study shows that, by and large, the ACS/WFC PSFs vary in a predictable way as a function of focus variation. These variations can be easily seen on a phylogram-like plot of the relative differences between the image-tailored empirical PSFs. At odds with the phylogram of the WFC3/UVIS (Anderson & Bedin 2017, e.g., their Fig. 6), the phylogram of the ACS/WFC is multi-modal on one side, with different tails of the distribution correlating with epoch, exposure time, the angle between the Sun and the V1 axis, and the altitude of the Sun above the Earth’s limb. Jitter RMS and the primary-use detector show no significant correlations with in the phylogram plot.

The process of constructing focus-diverse, spatially-variable PSF models started by collecting all suitable full-frame ACS/WFC images from the existing non-proprietary archive. The sample is divided according to the filter used. In addition, a distinction was made between pre- and post-SM4 observations, since both the shape of the PSFs and the geometric distortion of the ACS/WFC have changed since the camera was repaired during SM4. Phylogram plots were derived starting from the two most-commonly-used filters of the ACS/WFC: F606W and F814W. The phylograms are arbitrarily divided into regions of similar focus level, and a spatially-variable array of 9×10 PSFs is obtained for each region.

The QFIT parameter is used to verify that the new PSF are able to more closely match the actual shape of the stars in the images than the static library PSFs. The new PSFs provide similar results to what can be achieved by perturbing the library PSFs on an image-by-image basis, but without the need of hundreds of stars in the image. When enough stars are available on an image, the focus-diverse PSF models can be further refined via perturbation techniques.

A critical aspect of the new PSF models is that they minimize pixel-phase systematic errors that affect measurements made with the library PSF in extreme focus conditions.

Future analyses will comprise the construction of focus-diverse PSF models for the several other commonly used filters of the ACS/WFC. A handful of stars in an image will then be enough to identify the closest focus-diverse PSFs to the particular focus level of any image. These PSFs can then be interpolated to provide a precise set of PSF models for the particular focus of the image. The new focus-diverse PSF models will be compatible with the `hst1pass` software package (Anderson in preparation).

Far future plans involve the construction of an interactive web tool that, given an image and a position on either the `_flc` or the `_drc` files, returns the optimal PSF model for that position, resampled to the `_drc` pixel space if needed.

References

- Anderson, J., & King, I. R. 2000, *PASP*, 112, 1360
Anderson, J., & King, I. R. 2006, *ACS-ISR* 2006-01
Anderson, J., & Bedin, L. R. 2017, *MNRAS*, 470, 948
Bellini, A., Anderson, J., van der Marel, R. P., et al. 2014, *ApJ*, 797, 115
Bellini A., Anderson, J., Bedin, L. R., et al. 2017, *ApJ*, 84, 6
Di Nino, D., Makidon, R. B., Lallo, M., et al. 2008, *ACS-ISR* 2008-03
Hoffmann, S., & Anderson, J. 2017, *ASC-ISR* 2017-08
Niemi, S.-M., & Lallo, M. 2010, *ISR TEL* 2010-03
Sahu, K. C., Lallo, M., & Makidon, R. B. 2007, *ACS-ISR* 2007-12